Numerical and Experimental Investigation on Cyclic Behavior of Masonry Infill Walls Retrofitted with CFRP

Boudjamaa Roudane[1] · Süleyman Adanur[1,2] · Ahmet Can Altunişik[1,2,3]

Abstract

This paper presents verification of the numerical model of masonry infill walls against the experimental results. Three cases are investigated: an undamaged model, a damaged model, and a carbon fiber-reinforced polymer (CFRP) strip. ABAQUS commercial finite element model (FEM) software was used in the modeling. Nonlinear behavior as well as cracking and crushing of masonry bricks were simulated using the Concrete Damaged Plasticity (CDP) model. To solve this, a three-dimensional simplified micro-model was used. Experimental and simulation of the hysteresis curve, skeleton curve, damage patterns, maximum and minimum stresses, and plane strain distribution were compared. The changes in natural frequencies, and mode shapes before and after CFRP strengthening masonry wall are evaluated. A sensitivity analysis was done to study the effect of damage and strengthening on the nonlinear behavior of steel frames with masonry infill. This investigation demonstrated that the numerical model was able to effectively simulate and predict the strength of these models. Then a look at the effect on seismic performance is reported and commented on.

1 Introduction

The seismic behavior of masonry-infilled buildings has been a subject of investigation for the last half-century, with numerical and experimental studies concentrating on the interaction of infill walls with reinforced concrete (RC) and/or steel frame structures. Masonry walls are often applied as inner or outer walls in steel and reinforced concrete buildings, creating composite buildings known as infilled frames. These buildings indicate increased lateral stiffness and strength compared to those without walls, generally referred to as bare frames. The existence of walls made of stone considerably affects the performance of the bounding frames, particularly under seismic loading. Nevertheless, many building design engineers typically overestimate the importance of these infills, identifying them as nonstructural components, which can lead to incorrect outcomes. Over the last sixty years, a range of experimental and computational investigations [1–5] have been undertaken to develop rational approaches for accounting for the infill's contribution to the overall stiffness and strength of structural systems. The progress of computing technology over the past few decades has greatly improved the usage of numerical modeling, incorporated into specialized programs for modeling the behavior of masonry-infilled frames. This has been notably obvious in the carrying out of FEM [6–8]. The modeling of infilled frames has been greatly facilitated by discrete element methods [9, 10].

Significant numerical investigations have concentrated on studying the properties of steel frames made from material [4, 11, 12]. At the same time, there has been progress in laboratory studies on infilled frame structures,

✉ Ahmet Can Altunişik
ahmetcan@ktu.edu.tr

Boudjamaa Roudane
rou.ingc@ktu.edu.tr

Süleyman Adanur
sadanur@ktu.edu.tr

1 Department of Civil Engineering, Karadeniz Technical University, Trabzon, Turkey

2 Earthquake and Structural Health Monitoring Research Center, Karadeniz Technical University, Trabzon, Turkey

3 Dynamic Academy Software, Construction Ind. Trade. Co., Ltd. Şti, 61080 Trabzon, Turkey

particularly steel frames. This study has mainly focused on monotonic and cyclic quasi-static testing [13, 14] and, more recently, pseudo-dynamic testing [15]. Mehrabi et al. [16] develop interface models that describe the shear cracking in concrete and mortar joints, as well as the bond-slip behavior of steel reinforcement in concrete. Canbay [17], and Anıl and Altın [18] examined the cyclic behavior of RC infill walls through tests and static pushover analysis for verification. Darwish [19] and Sivri [20] conducted studies on the numerical modeling of RC infill walls subjected to cyclic loading, adopting parametric analysis. Lotfi and Shing [21] proposed a smeared crack model to simulate the nonlinear properties of masonry and concrete in infilled RC frames. Al-Chaar et al. [22] employed smeared crack quadrilateral elements to represent masonry and a cohesive interface model to simulate the behavior of mortar and shear failure in concrete. Stavridis and Shing [23] created a 2D micro-model for masonry-infilled RC frame analysis, adding cohesive crack interface features in order to simulate mortar impacts. Mohyeddin et al. [24] created a 3D micro-model, separating the mortar at joints and establishing an elastic interaction model between mortar layers. Minaie et al. [25] applied the Concrete Damaged Plasticity (CDP) model in ABAQUS to evaluate the one-directional loading behavior of whole and partially coated masonry shear walls. Kim and Yu [26] investigated the effects of masonry strength in infill walls on RC and steel frames subjected to lateral loads. The results revealed that infill RC frames exhibited higher residual strength, initial stiffness, and ultimate strength compared to frames without masonry infill walls. FE modeling of masonry infills divides into micro- and macro-modeling approaches. Micro-models enable a full description of masonry infills, producing exact behaviors. However, this approach needs massive processing resources, making it insufficient for larger structures. On the other hand, macro-models employ a more generalized representation of infill wall panels. This is often achieved by demonstrating the masonry infills as homogeneous isotropic walls or by replacing each infill panel with one or several diagonal struts. The selected method of analysis inside the FE frame considerably affects the cyclic behavior evaluation of masonry-infilled structures: macro-modeling [27–32] and micro-modeling [33–35]. The implicit method can be applied to a wide range of linear and nonlinear issues, requiring iterative strategies for each load increment to identify solutions. On the contrary, the explicit method is particularly suitable for short transient situations like impact loadings and is commonly applied in research. However, in analysis, the time dependence might create noise in seismic response assessments of structures, potentially leading to incorrect evaluations of the hysteresis behavior in steel plate walls, as reported by Azandarian [36]. Moreover, the addition of infill masonry walls provides additional failure mechanisms, such as short column effects, soft story phenomena, and torsional failures, which are commonly neglected in structural design [37]. Furthermore, the failure mechanisms of infilled frames have shown nonductile characteristics, as observed in studies like [38]. In order to improve our comprehension of how existing infill frames respond to seismic activity and develop efficient strategies for strengthening them, it is essential to employ dependable techniques for predicting the many failure modes that may occur during earthquakes. Numerous seismic retrofitting methodologies, such as steel bracing, column jacketing, and the application of FRP layers, are applied to improve the seismic resistance of infill structures. Recently, FRP has become popular as a modern option for building repair, given its multiple advantages, including a high strength-to-weight ratio, flexibility, and onsite customization. Batikha [39] have been studied about to improve both the load-carrying capacity and stiffness of FRP-RC masonry. For example, Yuksel et al. [40] and Ozkaynak et al. [41] validated that a retrofitting strategy involving cross-diamond bracing efficiently increases shear resistance, exceeding other methods. This method significantly reduces wall corner failures, where cracking commonly occurs under lateral loads. Additionally, Altin et al. [42] have seen a 50% increase in stiffness with the increase in CFRP strip thickness. Butenweg et al. [43] investigated complex nonlinear behavior in concrete infill walls and wall–frame interfaces, finding agreement useful for parametric studies and design recommendations. Finite element models using micro-modeling demonstrate good agreement. To address the weakness of masonry infills, Akın et al. [44] investigated FRP-strengthened infill walls using a numerical model. They validated simulation results by comparing results from OpenSees software with experimental response curves. A parametric study was conducted to further investigate the effect of the aspect ratio on hollow clay tile infill walls. The findings revealed that the use of diagonal CFRP strips significantly enhanced both the lateral strength and stiffness of the frames.

Similarly, other researchers have developed numerous strengthening techniques using different approaches and materials. These include the use of fiber-reinforced polymer (FRP) sheets [45], strengthening with FRP sheets and anchors [46], and strengthening with plaster mortar [47]. Although the aforementioned experimental investigation has contributed significantly to understanding the performance of steel frame interactions, the challenges and high expenses associated with conducting these tests, particularly for extensive parametric studies, have made FE modeling more common.

As a result, there is a pressing need for greater precision in numerical models to permit complete parametric

analysis. The experimental study conducted by Padalu et al. [48] demonstrated satisfactory performance in terms of strength, stiffness, ductility, and energy dissipation. The researchers compared the testing findings of RC frame samples with various types of infill strengthening materials, including FRP, fiber mesh, and wire mesh. Similarly, other researchers such as Leeanansaksiri et al. [49], Coccia et al. [50], Tanjung et al. [51], and Furtado et al. [52] focused their investigations on the strengthening of masonry infills. Various researchers have developed numerical models to evaluate the performance of masonry infill walls under both cyclic and monotonic loads, employing macro- and micro-modeling techniques. However, when observing the condition of masonry infill walls after earthquakes, it becomes evident that many problems and questions remain unsolved, necessitating further studies and development. The main challenge lies in representing the nonlinear behavior of elements and modeling the interaction between different materials, such as concrete and masonry. While previous numerical studies have demonstrated the capability of finite element (FE) models for simulating masonry infills or shear walls, some limitations have been identified. The use of 2D macro-models, although simple, proved inadequate in capturing various aspects of infilled frames, including nontypical geometric properties, stress concentration, local reinforcement effects, and out-of-plane behavior. In the case of existing 3D simplified micro-model studies, there is often a lack of information regarding input material parameters, making it challenging for others to replicate the model and reproduce the associated results.

Against this background, the purpose of this study was to conduct numerical analyses using Abaqus software and compare them with the findings of a previous experimental study on typical half-scale steel frames with brick masonry infill. For the current numerical analysis, a 3D finite element model was created to investigate the in-plane behavior of steel frames filled with. An investigation was conducted to examine the effects of different cases, including undamaged, damaged, and strengthened models. The results are discussed in the form of dynamic characteristics such as frequency values and mode shapes, load–displacement hysteretic curves, damage patterns, maximum and minimum principal stresses, and plane strain distribution. The complete validation of the model in contrast to the outcomes of the experiments was discussed. Also, the seismic performance of the damaged and strengthened models was determined.

2 Description of the Experimental Campaign

2.1 Test Setup

The structural behavior of steel frames with masonry infills was analyzed in this study using experimental tests conducted by Samberou [53]. A 1/2-scaled, single-story rectangular infilled steel frame was cast for this purpose. The model comprises two W250 × 58 columns and one W200 × 46 beam, with a height of 1500 mm and a span of 1200 mm. The height/length ratio is approximately 1.25:1. The brick infill has dimensions of 185 mm (length), 285 mm (height), and 100 mm (thickness). The dimensions of the model. The experimental test and the hollow brick units are depicted in Fig. 1. The construction of the model involved single-wythe masonry walls as infill, and the experimental tests subjected the model to reversible and repeated horizontal loads. Experimental measurements were carried out using ambient vibration tests [54, 55].

2.2 Lateral Loading Cycles

Figure 2 depicts the application of a displacement control loading approach in the current study. The loading methodology was established in conformity with FEMA 461 [56]. A low-cycle cyclic load was applied to the centroid of the top frame beam.

This load is frequently used for seismic performance assessment of nonstructural components, enabling the measurement of all levels of damage to develop appropriate fragility models [57].

Three different cases are taken into account to simulate the states that include intact, impaired, and reinforced. The undamaged infill wall is designated as Model-W0, the damaged as Model-W1, and the strengthened with CFRP strip as Model-W2. The experimental testing consisted of applying cyclic loadings to the masonry infill wall, with a range of −100 to 100 kN (Fig. 3).

3 Description of the Numerical Simulation Approach

This study has concentrated on the numerical verification of three different model cases: the undamaged infill model (Model-W0), the damaged infill model (Model-W1), and the infill frame strengthened with CFRP strips. The FE modeling in this study adopts ABAQUS [58]. An advanced nonlinear software package known for numerous material constitutive laws and strong contact features is perfect for simulating brick infill walls. This commonly utilized
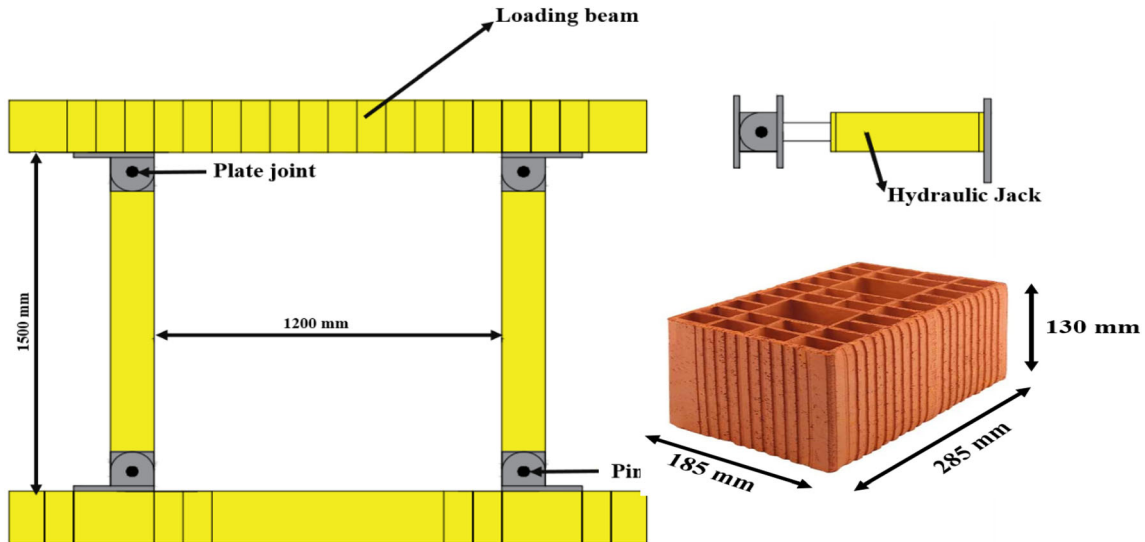
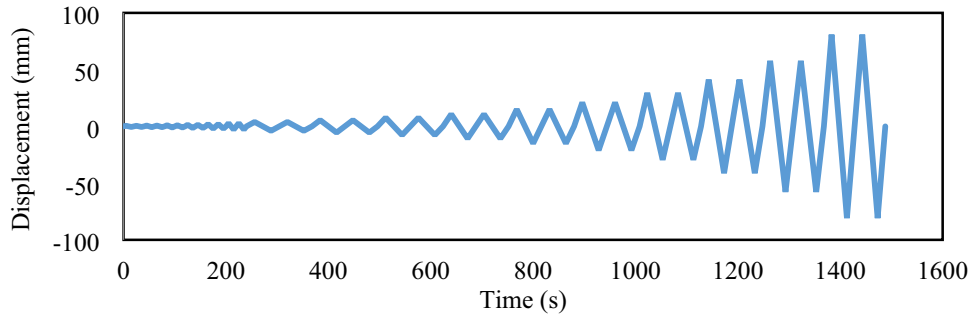**Fig. 1** Front view geometry of the steel frame and hollow brick dimensions [39]

Fig. 2 Applied horizontal displacement protocol (FEMA 461) [40]

Fig. 3 With and without CFRP strengthening experimental models [53]

commercial FE software simulates modal analyses and cyclic nonlinear quasi-static analyses. The subsequent parts detail the structure of geometry, the meshing procedure, constitutive material models, and the particulars of the numerical studies.

3.1 Definition of Materials

The material properties utilized in the analysis were selected based on findings from literature studies investigating similar materials. For brick units, the elasticity

modulus and density values were considered within the ranges of 3.5–34 GPa and 1200–2000 kg/m² respectively [59, 60]. The mechanical properties of the steel profiles were obtained from ASTM-A36 [61]. Both linear elastic and nonlinear material properties employed in the analyses are detailed in Table 1.

The literature includes a number of constitutive models based on the fundamental concepts of elasticity, plasticity, and continuum damage mechanisms. In this study, the Concrete Damaged Plasticity (CDP) model is applied to evaluate the mechanical properties of bricks, based upon the micro-modeling approach initially proposed by Lourenco [63] and further improved by Lourenço et al. [64]. This modeling approach is particularly suitable for simulating isotropic brittle materials, such as masonry units, as demonstrated by Moradabadi et al. [64] and Page [65]. CDP was chosen to represent the tensile behavior of the masonry infill wall [66]. The damage parameters and variables in the CDP model are based on the assumption that damage occurs only in the softening range [67]. The specific values of the parameters in the CDP model may vary based on the type of concrete being modeled and the loading conditions. Therefore, it is advisable to calibrate the CDP model parameters using experimental data before employing them in numerical simulations [68]. The CDP model can be implemented in ABAQUS to analyze concrete and other quasi-brittle materials, and it stands as one of the most widely used models for simulating concrete's nonlinear behavior [69]. Modal analysis and nonlinear time history analysis were conducted to assess the structural performance of each minaret. In the nonlinear analyses, the CDP material model was employed. This constitutive model combines plasticity theory and damage mechanics, assuming that the main failure mechanisms of the material are tensile cracking and compressive crushing. The evolution of the yield (or failure) surface is controlled by two hardening variables, ε_t^{pl} and ε_c^{pl}. Where, ε_t^{pl} and ε_c^{pl} linked to failure mechanisms under tension and compression loading and refer to as tensile and compressive equivalent plastic strains, respectively. These variables are referred to as tensile and compressive equivalent plastic strains, respectively. The stress–strain diagrams of the CDP model,

adaptable to masonry structures to define nonlinear material behavior, are presented in Fig. 4.

The stress–strain response exhibits a linear elastic relationship under uniaxial tension until reaching the peak stress, σ_{t0}. The initiation of micro-cracking in the material corresponds to the peak tension stress. Subsequently, the stress–strain response is characterized by material softening. Under uniaxial compression, the stress–strain response follows a linear elastic relationship until reaching the initial yield value, σ_{c0}. The plastic regime is marked by stress hardening, followed by strain softening beyond the ultimate stress, σ_{cu}. The stress–strain relations under uniaxial tension and compression loading are defined in Eqs. 1 and 2.

$$\sigma_t = (1 - d_t)E_0(\varepsilon_t - \varepsilon_t^{pl}), \qquad (1)$$

$$\sigma_c = (1 - d_c)E_0(\varepsilon_c - \varepsilon_c^{pl}), \qquad (2)$$

In these equations, ε_c and ε_t represent the total strain in compressive and tension conditions, E_0 is the initial modulus of elasticity, σ_c and σ_t are compressive and tension stresses, and d_c and d_t are compressive and tension damage parameters, respectively.

The stress–strain behavior of brick masonry is indicated in Fig. 5. The stress–strain response follows a linear elastic relationship under uniaxial tension until the peak stress σ_{t0} is reached, indicating the initiation of micro-cracking. After reaching the peak tension stress, the material exhibits softening. To address the issue of convergence difficulties encountered when elements exhibit softening behavior, the factor μ_v is introduced. This parameter plays a critical role in stabilizing the numerical model and ensuring reliable convergence during the simulation of softening responses in materials [70]. In implicit analysis, material models that display softening behavior and stiffness degradation can frequently result in significant convergence challenges. This approach modifies the consistent tangent stiffness of the softening material to maintain a positive value, particularly when sufficiently small time increments are used. This method is crucial for ensuring stability and accuracy in simulations involving materials with softening characteristics (Tables 2 and 3).

Table 1 Linear elastic material properties used in FE analyses [62]

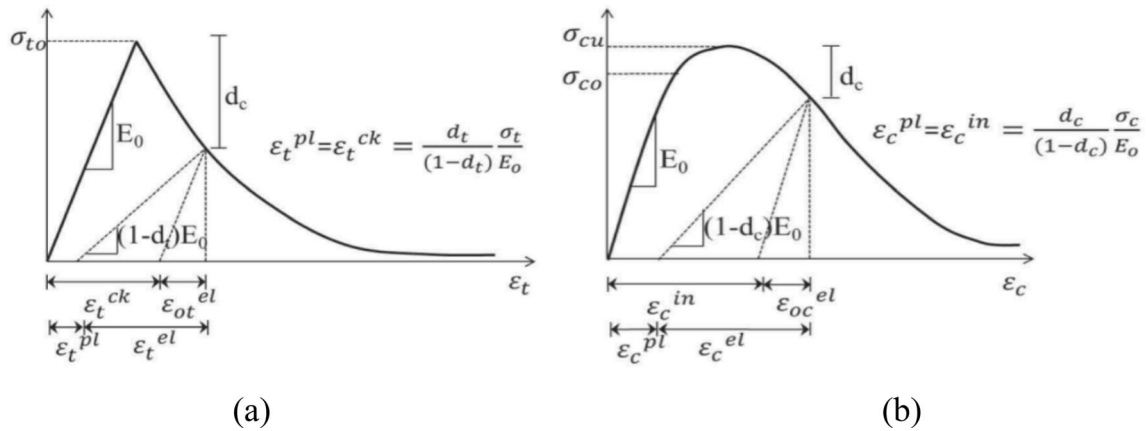| Material	Young's modulus (MPa)	Density (kg/m³)	Poisson's ratio (–)	Compressive strength (MPa)	Tensile strength (MPa)
Brick units	16700	1600	0.20	5	0.22
Mortar	2802.8	–	0.20	2.80	0.15
steel frame	200000	7700	0.30	–	–
CFRP layer	230000	–	0.20	–	

Fig. 4 Response of material to uniaxial **a** tension and **b** compression [63]
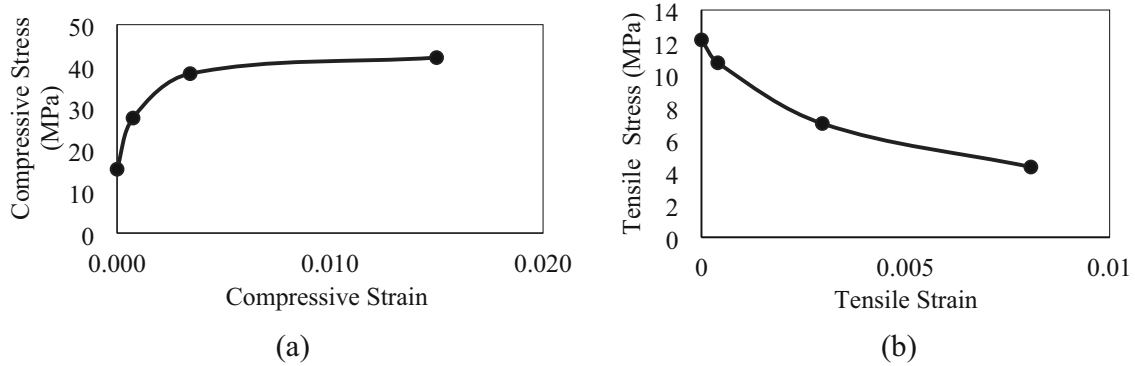

Fig. 5 Stress–strain properties of brick unit: **a** compression and **b** tension [63]

Table 2 Mechanical parameters of CDP model used in brick wall [63]

Dilation angle	Eccentricity	fb_0/fc_0	K_c	μ_v
30	0.1	1.16	0.67	0.002

Table 3 Compression and tensile stress–strain values of brick wall [63]

Compression		Tension		Damage parameter	
σ_c (MPa)	ε_c^{pl}	σ_t(MPa)	ε_t^{pl}	dc	dt
15.32	0	0	12.16	0	0
22.7	1.25E−04	2.85E−02	10.75	4.02E−05	3.85E−01
38.25	3.43E−03	4.53E−01	7.01	2.96E−03	9.00E−01
42.10	7.55E−03	8.89E−01	4.33	8.07E−03	9.96E−01

Fig. 6 Constitutive model for CFRP strip [71]

In this study, the CFRP material is modeled as a linear elastic isotropic material through the moment of failure, showing negligible yielding when compared to steel reinforcemen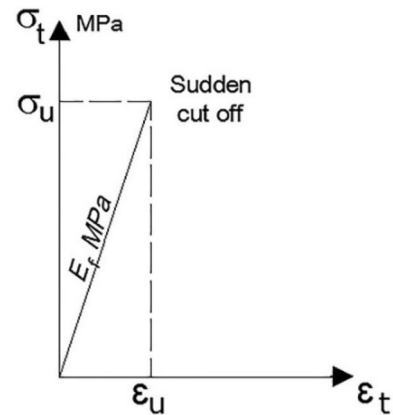t. Figure 6 depicts the selected model, in conjunction with its parameters: E_f represents the elastic modulus of the fiber; σ_{fu} is the ultimate stress of the fiber; and ε_{fu} is the tensile failure strain of the fiber. The above method of modeling CFRP material represents its particular mechanical characteristics, especially its linear elastic response until failure.

3.2 Contact Model

The cohesive interaction in materials has been defined as a function of the displacement separation between the edges of potential cracks [72]. Permeability studies have also been conducted to investigate the parameters that affect the performance of cohesive interaction in loose materials. The studies suggest that the mechanical behavior of cohesive elements can be described in three modes: (1) based on uniaxial stress, (2) based on continuity, and (3) based on a tension-separation structural model. The traction-splitting pattern represents the corresponding initial separation caused by the normal stress (Fig. 7).

The mortar was not explicitly modeled in the numerical simulation. Contact elements are used at the interfaces of the bricks to allow for the presence of the mortar. The contact elements employ a cohesive surface-based behavior that models the mortar joints using traction separation of the interfaces [5]. This approach allows for a linear elastic transmission of compressive stresses, tensile stresses, and shear stresses until the maximum strength of the mortar is reached. In addition to maximum strength, friction that contributes to the shear stress is activated. For the transfer of compressive stresses, a hard contact method is used whenever the surfaces are in contact.

3.2.1 Definition of Interaction

The constitutive behavior of masonry bricks and interfaces was defined using material models. The present study employed nonthickness cohesive elements. The linear elastic traction separation law prior to damage is written in terms of the tractions, t, and separations, δ, constitutive matrix, as shown in Eq. 3.

$$t = \begin{Bmatrix} t_n \\ t_s \\ t_t \end{Bmatrix} = \begin{bmatrix} K_{nn} & K_{ns} & K_{nt} \\ K_{ns} & K_{ss} & K_{st} \\ K_{nt} & K_{st} & K_{tt} \end{bmatrix} \begin{Bmatrix} \delta_n \\ \delta_s \\ \delta_t \end{Bmatrix}. \tag{3}$$

In the context provided, the nominal traction stress vector t comprises three components: t_n, t_s, and t_t, which represent the normal and two shear tractions, respectively. Corresponding to these tractions are the associated separations, δ_n, δ_s, and δ_t. The stiffness of the interface, denoted as K, is expressed in Eqs. 4 and 5. This definition of K is crucial in modeling the behavior of the interface, particularly in relation to the tractions and separations.

$$K_{nn} = \frac{E_u E_m}{h_m(E_u - E_m)}, \tag{4}$$

$$K_{ss} = K_{tt} = \frac{G_u G_m}{h_m(G_u - G_m)}. \tag{5}$$

In the given context, E_u and E_m represent the Young's modulus, while G_u and G_m are the shear modulus for the block and mortar, respectively. Additionally, h denotes the actual thickness of the mortar layer. The validity of this methodology has been corroborated in [73] study, through detailed discontinuum finite element analyses. In this study, the tensile strength (t_n^{max}) and shear strengths (t_s^{max}) and (t_t^{max}) were calibrated based on the diagonal compressive testing of masonry triplets, as reported in [15], employing the formulas presented in Eq. 6. This calibration process ensures that the model accurately reflects the mechanical properties of the materials used in masonry construction.

$$\left(\frac{t_n}{t_n^{max}}\right)^2 + \left(\frac{t_s}{t_s^{max}}\right)^2 + \left(\frac{t_t}{t_t^{max}}\right)^2 = 1. \tag{6}$$

The initial behavior of the element is assumed to be linearly elastic. This is followed by the initiation and progression of the damage. The criteria for damage initiation and propagation are defined by the mixed modes of tensile behavior (Mode I) and shear behavior (Mode II). The quadratic stress criterion is adopted for the initiation of the damage.

Damage evolution is linear, and the shrinkage and shear fracture of the mortar joint depend on the energy release
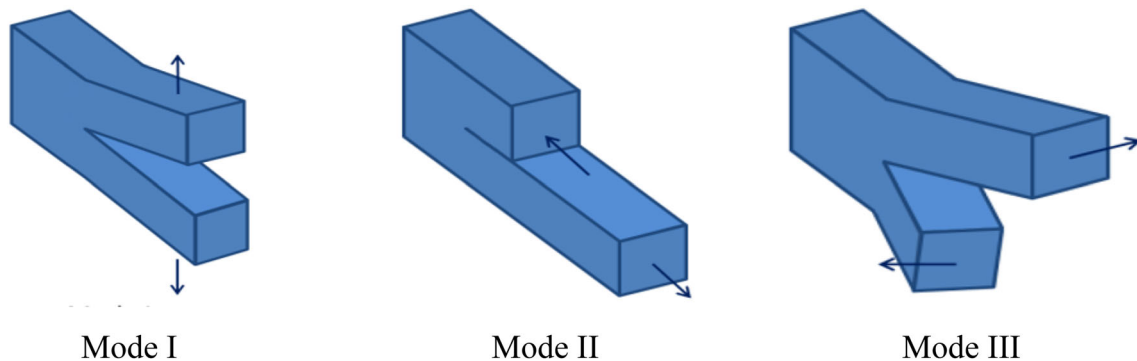

Mode I · Mode II · Mode III

Fig. 7 The view of three traction-splitting patterns

Table 4 Properties of interfaces between brick units and infill to frame [66]

Contact			Interaction	
Cohesive behavior			Brick–Brick	Infill–frame
Stiffness	Normal stiffness (K_{nn})		70	11
	Shear stiffness (K_{ss})		40	11
Damage	Initiation (N/mm^2)	*Normal* (t_{nn})	0.23	0.10
		Shear I (t_{ss})	0.15	0.15
		Shear II (t_{tt})	0.15	0.15
Evolution	Fracture energies (Nmm/mm^2)	G_c^f	0.3	/
		G_f^I	0.025	/
		G_f^{II}	0.5	/
	Plastic displacement (mm)		/	1
	Exponential parameter		2	10
	Tangential behavior		0.75	0.57
	Normal behavior		Hard contact	Hard contact

rate G_I and G_{II}. These fracture shrinkage energy rates were estimated based on the [21] study. According to the Benzeggagh and Kenane criterion [74], when the shear failure energy velocity is reached, the fracture of the mortar joint has occurred. In the simulation investigation, the mortar interfacing the bricks is considered a cohesive surface interaction, providing a variety of interface elements, notably cohesive elements that are frequently used to define bonded or sliding phenomena, as noted by Diehl [75].

These cohesive features are divided into two distinct categories: element-based and surface-based cohesive elements, both capable of performing the behavior of mortar joints. In the study conducted by Aref et al. [76], element-based cohesive elements were used, combining a set of users' constitutive models to precisely represent the cyclic behavior of mortar.

3.2.2 Type of Contact

This study includes the interaction between steel and masonry walls, applying friction as an important component. The model combines tangential behavior and the concept of "Hard" contact, allowing no softening and no penetration between surfaces. The friction coefficients are chosen to properly illustrate the materials involved, with 0.75 for brick masonry and 0.57 for brick-to-steel contact, providing the most accurate representation of the physical interactions in the investigation. The properties of interfaces between bricks and infill to frame joints are listed in Table 4.

On the other hand, the mortar joints between adjacent masonry units are modeled using contact pairs, an approach referred to as "simplified micro-modelling" in the

literature. This method strikes an optimal balance between simulation accuracy and computational efficiency, contrasting with the more intricate "simplified micro-modelling" technique where mortar joints are explicitly modeled [2]. The interactions between the bricks themselves, however, are represented by zero-thickness interface interactions. This methodological choice is pivotal in accurately depicting the mechanical behavior of masonry structures while maintaining computational manageability.

The "General Contact" interaction technique in ABAQUS was applied to simulate the interactions between steel frames and masonry infill walls, as well as among masonry units following mortar joint failure. This technique successfully captures the linear relationship between shear and normal forces on contacting surfaces, therefore generating frictional forces at the boundaries of these surfaces. For this
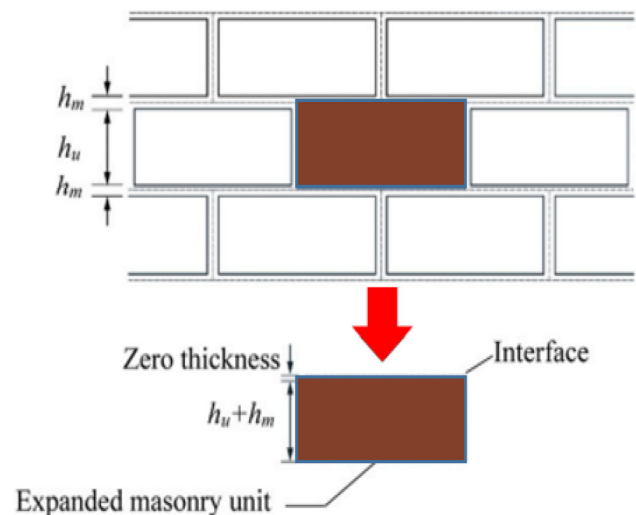
Fig. 8 Simplified micro-modeling of masonry brick [77]

purpose, the friction coefficient μ was chosen at 0.4. The interactions between the bricks themselves, however, are represented by zero-thickness interface interactions, employing contact components as shown in Fig. 8. This methodical approach is crucial for accurately capturing the mechanical behavior of masonry structures while maintaining computational efficiency.

3.3 FE Modeling

3.3.1 Interaction of CFRP–Wall

The CFRP in the FE model is represented using shell elements. In the experimental test, the FRP was seen to attach effectively to the damaged masonry wall, with no signs of surface deboning from either the masonry wall or the steel frame. Consequently, in the numerical study, the surface interactions between the CFRP and the masonry wall are established using a tie constraint. In this configuration, the wall surface operates as the master surface, while the CFRP is designated as the slave surface. This approach ensures a robust and accurate depiction of the strengthening case in the model. The CFRP-strengthened model is represented in Fig. 9.

3.3.2 Type of Boundary Conditions and Loading

In the numerical models, horizontal loads were applied to the beams as per the experimental tests. FE model's schematic is illustrated in Fig. 10a, where horizontal excitation is applied monotonically to the upper flange of the steel beam. Fixed boundary conditions, as shown in Fig. 10b, are obtained by restricting both translational and rotational movements at all nodes on the bottom of the
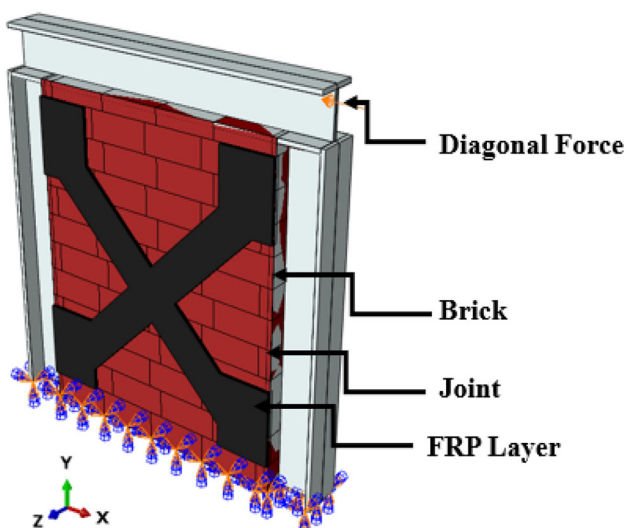

Fig. 9 ABAQUS model of the CFRP-strengthened case

model. To replicate real-world loading situations and avoid the effects of abrupt peak loading, the load was applied monotonically with a smooth amplitude. Furthermore, the model includes geometric nonlinearity to describe the real in-plane behavior of the masonry infill wall models under load. All interactions between beams and columns are assumed to be rigid, with any damages or fractures at these connections not considered in the analysis. The interactions between the steel columns and beams are established using tie constraints, guaranteeing that the load transmission mechanism is appropriately represented.

3.3.3 Type of Element and Meshes

In the modeling process, brick units were represented using eight-node three-dimensional components with reduced integration and a Gaussian integration point (C3D8R). The steel frame and CFRP strips were modeled using four-node shell elements (S4R). To establish the appropriate mesh size and type, mesh sensitivity analyses were done. To achieve an equilibrium between computational effectiveness and precision, multiple mesh sizes were chosen for various structural components. Specifically, a coarser mesh of 100 mm was chosen for the T-shaped steel beam. In contrast, more precise meshes were utilized for the infill and columns, with sizes of 40 and 60 mm, respectively. This mesh size was demonstrated to be sufficient for accurate findings and appropriate analysis time through mesh convergence research. The same mesh size was extended to the CFRP. The chosen mesh arrangements for both the masonry-infilled RC frame and the brick units are presented in Fig. 11.

For the representation of the masonry infill wall's behavior, a homogenized, simplified micro-modeling approach was used [78, 79]. This micro-model is especially important for our investigation, which focuses on the accurate behavior of infilled frames, demanding a comprehensive nonlinear analysis.

3.3.4 Type of Analysis and Convergence

In this verification study, two types of analysis were conducted: modal analysis and nonlinear cyclic analysis. The nonlinear cyclic analysis was done in two phases using numerical model. In the first step, the structural self-weight and additional dead loads were applied. The second phase involved a quasi-static analysis via explicit solver, material nonlinear analysis. The ability of ABAQUS for such analyses has been verified in numerous analytical and numerical studies [81–84]. However, it is noteworthy that highly nonlinear problems, like those modeling masonry buildings, typically have challenges in FEM solutions, including convergence difficulties and premature
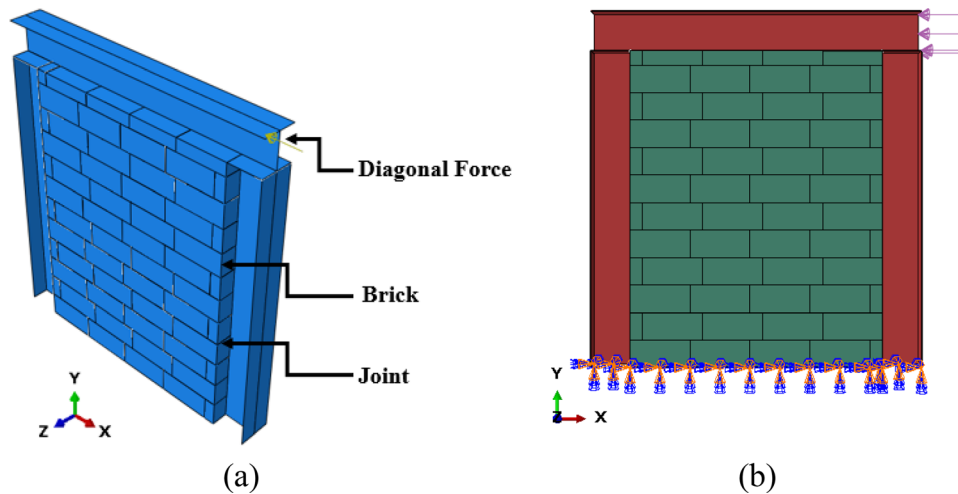
Fig. 10 ABAQUS model **a** model geometry and **b** boundary conditions
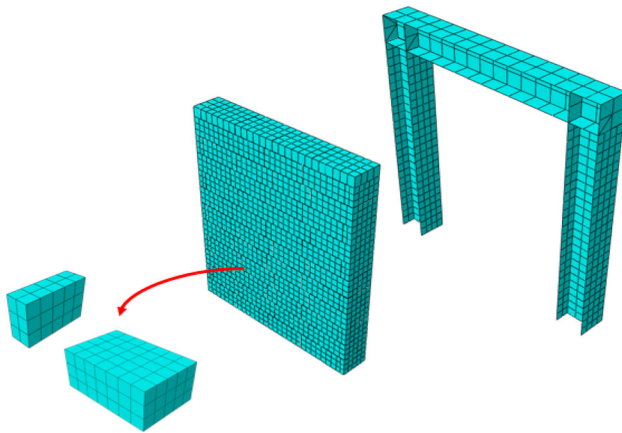

Fig. 11 Generated mesh of the model

termination of the solution in the early phases of the non-linear regime. The current study focuses on the application of explicit analysis utilizing ABAQUS software. This method is crucial for ensuring stability and accuracy in simulations involving materials with softening characteristics.

4 Results and Discussion

4.1 Modal Analyses

In this section, three different cases (undamaged, damaged, and strengthened) are considered for the masonry-infilled steel frame model to show the changes in dynamic characteristics. This is one of the most important analyses to demonstrate the accuracy of the FE model. However, the FE model includes many uncertain parameters, such as material property, boundary condition, mesh size, element type, and modeling assumptions. For this reason, it is

Table 5 The first three frequency values for each case obtained by numerical and experimental methods

Mode	Frequencies (Hz)		Diff. (%)	Av. Diff. (%)
	Numerical	Experimental		
Undamaged Infill Wall Model/Model-W0				
1	12.47	12.62	1.19	0.74
2	25.27	25.02	1.00	
3	38.35	38.36	0.03	
Damaged Infill Wall Model/Model-W1				
1	9.84	9.39	4.57	3.87
2	21.64	22.45	3.74	
3	36.25	37.51	3.47	
Strengthened Infill Wall Model/Model-W2				
1	15.47	15.37	0.65	0.99
2	29.00	29.51	1.73	
3	41.83	41.58	0.60	

necessary to verify the numerical results with experimental measurement and reduce the possible differences to acceptable limits by using a model updating approach. Table 4 summarizes the numerical and experimentally identified first three frequency values for undamaged, damaged, and strengthened masonry infill walls. It can be seen that there is a good agreement between numerical and experimental results; the average differences were calculated as 0.75% for Model-W0, 3.87% for Model-W1, and 0.99% for Model-W2. Significant decreases in frequencies occurred with the damage. The maximum reduction was calculated as approximately 21% in the second mode. After the strengthening, there was a significant increase in the frequencies. Compared to the damaged state, the maximum increase percentage is set at about 36% in the first mode. It

Table 6 The first three mode shapes for each case

Method	First mode Transverse in-plane	Second mode Torsion in-plane	Third mode Out-of-plane
	Undamaged Infill Wall Model/Model-W0		
Experimental			
Numerical			
	Damaged Masonry Infill Wall Model/Model-W1		
Experimental			
Numerical			
	Strengthened Masonry Infill Wall Model/Model-W2		
Experimental			
Numerical			

is seen that the strengthened model becomes more rigid than the undamaged condition. The first three frequency values for each case obtained by numerical and experimental methods are summarized in Table 5.

The numerical and experimental first three mode shapes are depicted in Table 6. The first mode is transverse mode in-plane, followed by torsion mode in-plane, and finally out-of-plane mode. It can be seen that the numerical and experimental mode shapes obtained for the undamaged,

damaged, and strengthened cases are in harmony with each other. It has been observed that the mod shapes obtained for the damaged and undamaged scenarios are the same, and there is no change in the mod shapes after the damage. However, after the strengthening, the 1st and 3rd mode shapes have changed places. Table 6 shows the first three mode shapes for each case obtained by numerical and experimental [53].
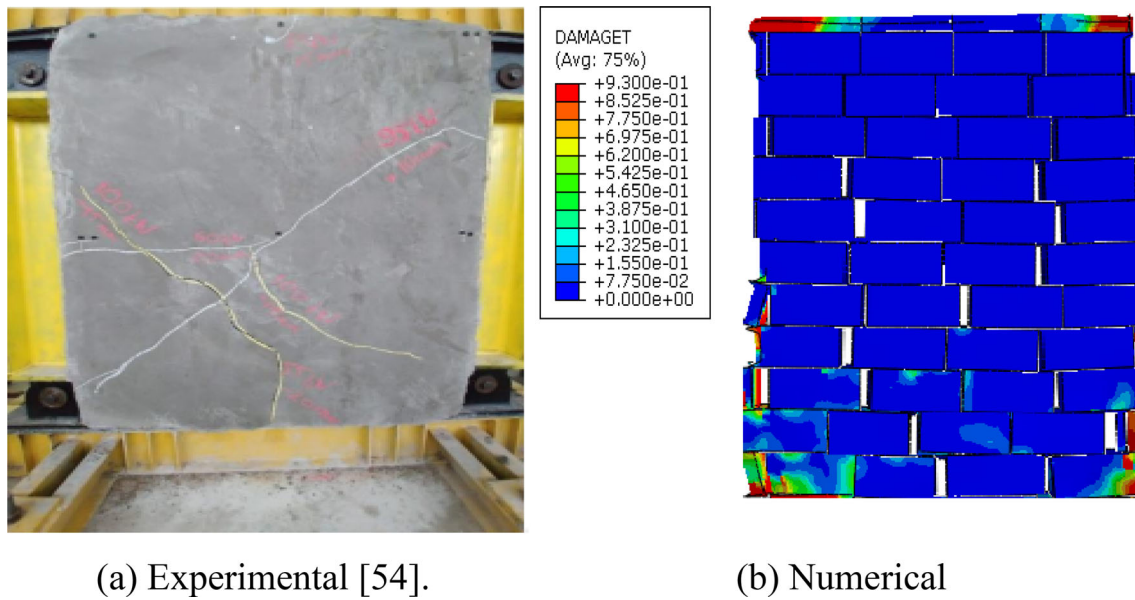
(a) Experimental [54].   (b) Numerical

Fig. 12 Comparison of damage patterns for damage case between test and FE results. **a** Experimental [53]. **b** Numerical

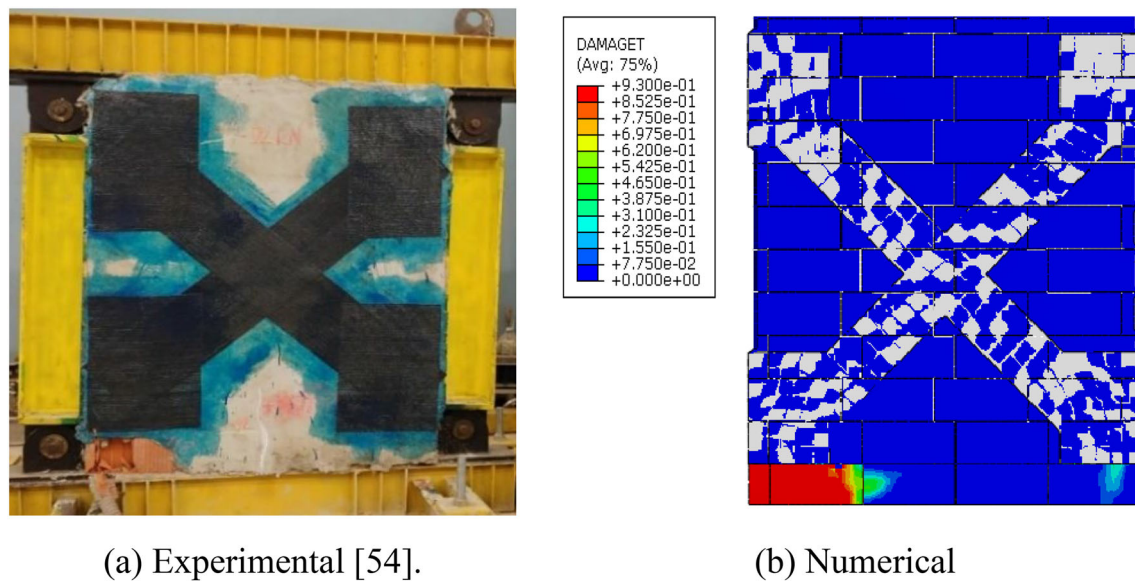(a) Experimental [54].   (b) Numerical

Fig. 13 Comparison of damage patterns for strengthening case between test and FE results. **a** Experimental [53]. **b** Numerical

4.2 Nonlinear Analyses

The numerical simulations carried out for this investigation contained two important steps: modal analysis and cycle analysis. Figures 12 and 13 present comparative findings between the outcomes of previous experimental testing and the simulated damage patterns for the damaged and strengthened cases, respectively. As indicated in Fig. 12, a comparison between the experimental test results and the FEM of Model-W1. The masonry infill wall was characterized by diagonal and transverse cracking at the horizontal mortar joints. Particularly, the diagonal cracks were

mainly situated at the upper right and lower left corners of the brick masonry infill wall, as depicted in Fig. 12b. After to the application of CFRP strips, damage took place mainly in the bottom left corner of Model-W2, as shown in Fig. 13b. It is particularly important to cracking that estimating the extent of damage in a CFRP-strengthened infill wall through visual examination alone can be challenging, especially in cases of small failures. In the simulation results, areas highlighted in red indicate where the stress surpassed the cracking or tensile strength, while green areas indicated imminent cracking or failure. The present pattern corresponds well with the quasi-static test results.
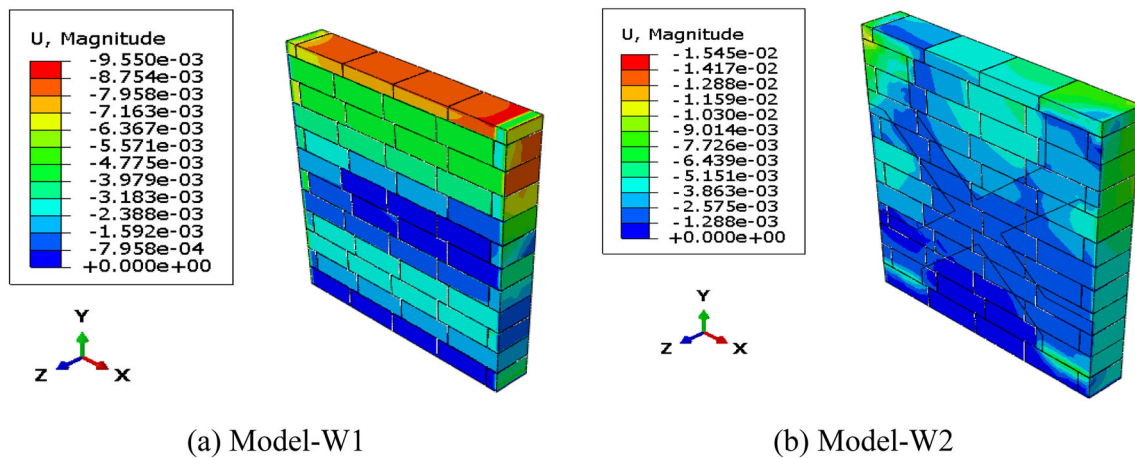
(a) Model-W1

(b) Model-W2

Fig. 14 Maximum displacement contour diagram (in m unit). **a** Model-W1. **b** Model-W2
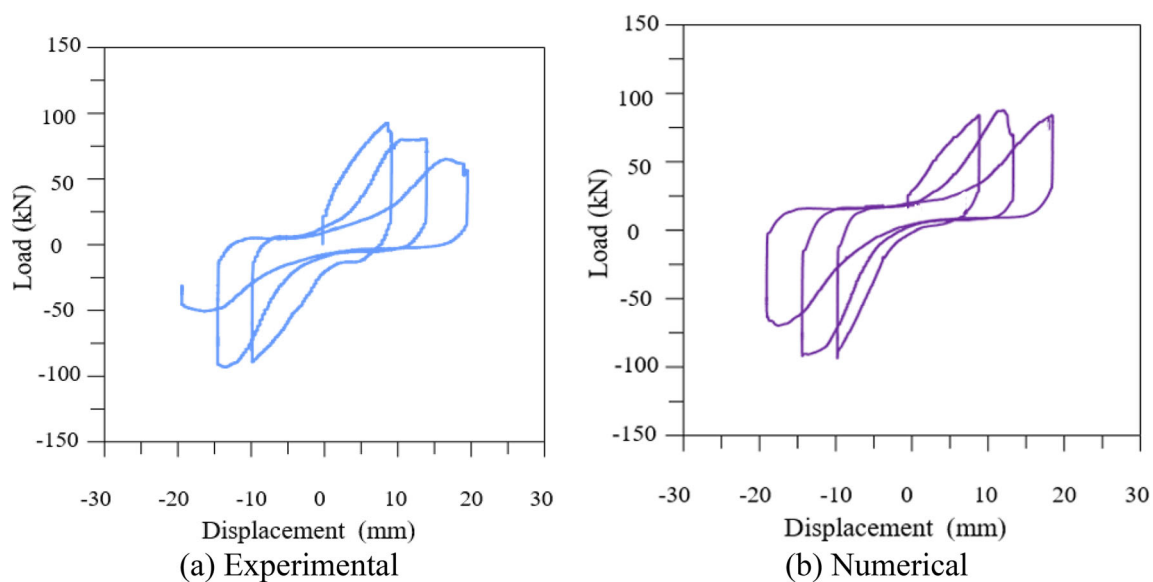

(a) Experimental

(b) Numerical

Fig. 15 Experimental by Samberou [53] and numerical results of the Model-W1. **a** Experimental. **b** Numerical

The agreement between the actual numerical simulation results and experimental findings data demonstrates the efficacy of the simplified micro-modeling approach applied in the FE study. This approach successfully replicated the practical in-plane behavior observed in the damaged and strengthened models. In all models, corner crushing appeared as the ultimate failure mechanism, typically following the development and propagation of diagonal cracking. This knowledge is crucial for understanding the failure mechanisms of masonry infill wall under different load scenarios.

Figure 14 displays the displacement contours of the infill masonry wall model in two different cases: with and without CFRP strengthening. This component of the study examines the impact of applying CFRP strips on the performance of Model-W2 when subjected to cyclic loading.

The results, as represented in Fig. 14b, reveal a significant reduction in wall displacement by about 62% related to the addition of CFRP strips. This study points out the beneficial effects of CFRP strips on increasing the structural strength of masonry walls against loads, indicating their potential as a possible strengthening solution.

Figures 15 and 16 provide a comparison study between the outcomes of previous tests and the simulated hysteretic curves for both damaged and strengthened cases, respectively. Achieving aspect of this comparison is mostly due to the absence of experimental data in its raw form. Despite this, the approach used permits for an accurate and clear comparison, even without the data being displayed on the same graph. The hysteretic and backbone curves are crucial in assessing the nonlinear seismic response of the models, since they offer insights into the strength and deformation
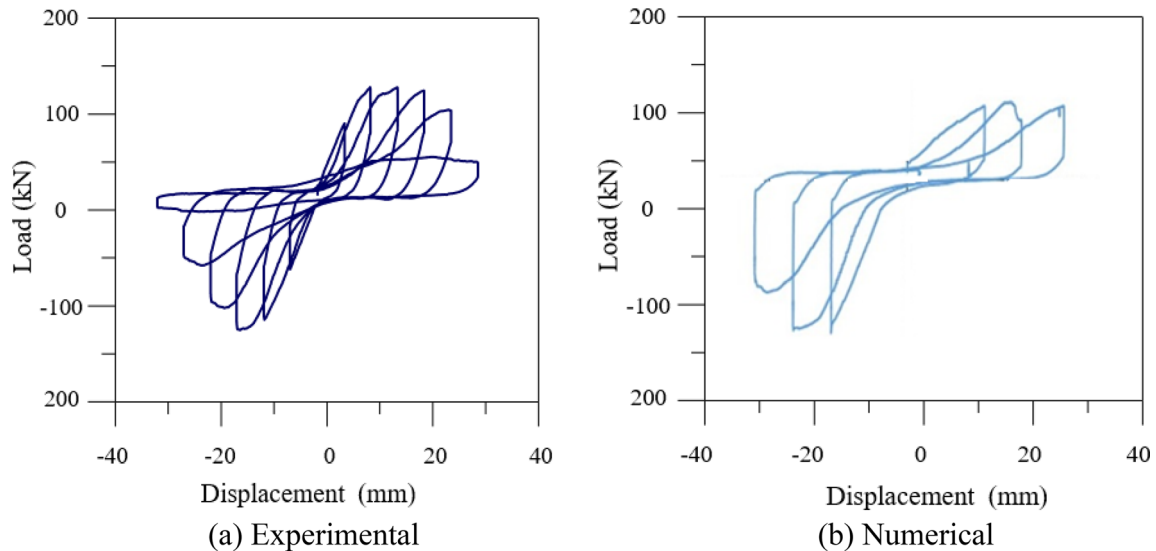
Fig. 16 Experimental by Samberou [53] and numerical results of the Model-W2. **a** Experimental. **b** Numerical
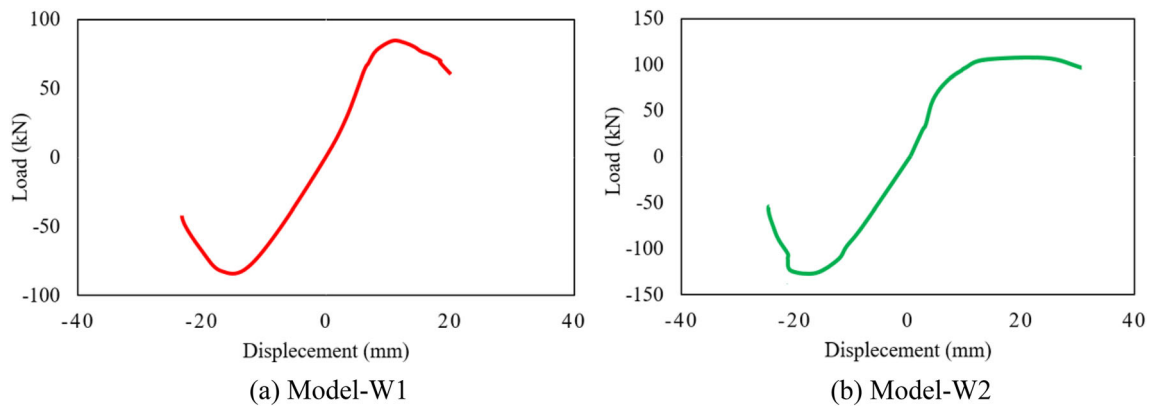

Fig. 17 Numerically obtained backbone curves of infill wall models. **a** Model-W1. **b** Model-W2

Table 7 Numerical and experimental load-carrying capacities and the maximum displacements

Model	Characteristic values	Numerical	Experimental	Diff. (%)
W-1	Load-bearing capacity (kN)	−96.37	−100	3.63
	Max. displacement (mm)	−9.55	−9.5	0.53
W-2	Load-bearing capacity (kN)	−136.62	−140	2.86
	Max. displacement (mm)	−15.45	−15	3.00

properties. Figures 15a and 16a illustrate that before yielding, both FE models displayed a constant increase in load-carrying capacity with displacement, minimum residual deformation, and no significant stiffness loss. However, as the displacement increased, cracking developed. Post-yielding, the hysteretic curve of both models demonstrated an "arc" shape, with pinching effects due to the opening and closing of cracks in the FE models.

A finding is that the hysteretic curves of the simulated and experimental models closely coincide, verifying the robustness of the FEM. Differences in the shape of these curves could be attributable to the weak restricting during the experimental test. Figure 15 depicts comparisons of representing and predicted the cyclic load–displacement curves with the numerical results for Model-W1. It is notable that the peaks on the graph are at 96 and −96 kN. The initial peak is attained at a displacement close to
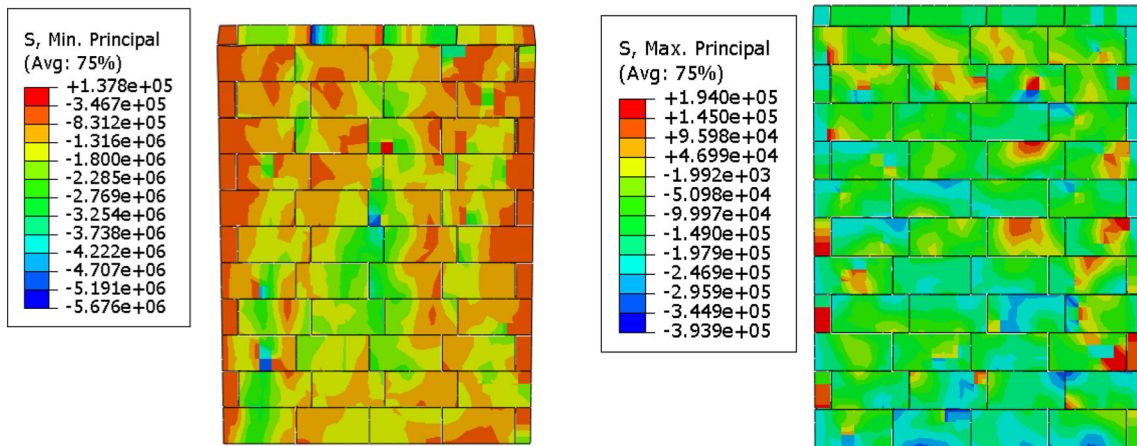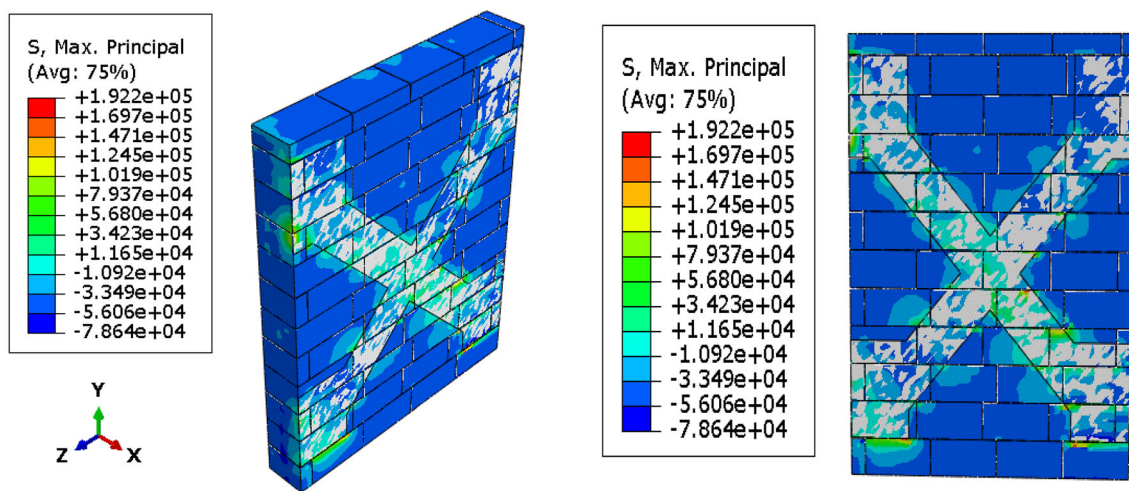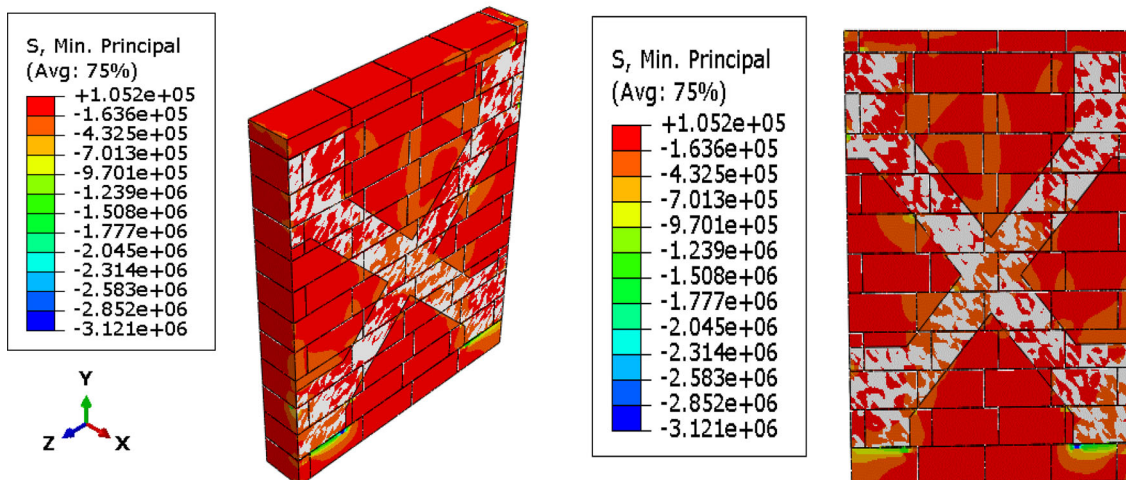
Fig. 18 Maximum and minimum principal stress of Model-W1 numerically obtained, in Pa

(a) Maximum principal stress

(b) Minimum principal stress

Fig. 19 Maximum and minimum principal stress of Model-W2 numerically obtained, in Pa. **a** Maximum principal stress. **b** Minimum principal stress

9.5 mm, aligning closely with the 9.55 mm displacement observed in the micro-modeling analysis, resulting in a minor error margin of 0.3%. Subsequently, the final tensile peak is observed when the force approximates 60 kN, coinciding with a displacement of 18 mm.

Figure 16 illustrates comparisons of representing and predicting the cyclic load–displacement curves for Model-W2. In the graph on the wall, it is indicated that a displacement of approximately 17 mm corresponds to around 13 kN. However, the initial peaks occur at about 136.62 kN for displacements of 15.45 mm in compression. In tension, the first peak is achieved with less than 18 mm of displacement. As the forces are absorbed, the wall weakens, resulting in the second peak being observed at 130 kN for a displacement of 25 mm. Regarding tension, the last peak occurs at 95 kN with a displacement of approximately 32 mm.

Figure 17 illustrates the backbone curves for Model-W1 and Model-W2, derived from the hysteretic cyclic loading data. The bearing capacity is obtained by connecting the peak points of the load–displacement graphs derived from the numerical simulation. By comparison, the backbone curve of the strengthened wall in Fig. 10b is significantly higher than that of the damaged wall in Fig. 10a. Similar behavior of bearing capacity is described in the literature [85].

To further aid in understanding and distinctly comparing the load-bearing capacity and maximum displacements before and after damaged and strengthened models. Table 4 shows the ultimate load damaged and strengthened models and the displacement value under the ultimate load obtained by simulation result and experimental finding (Table 7).
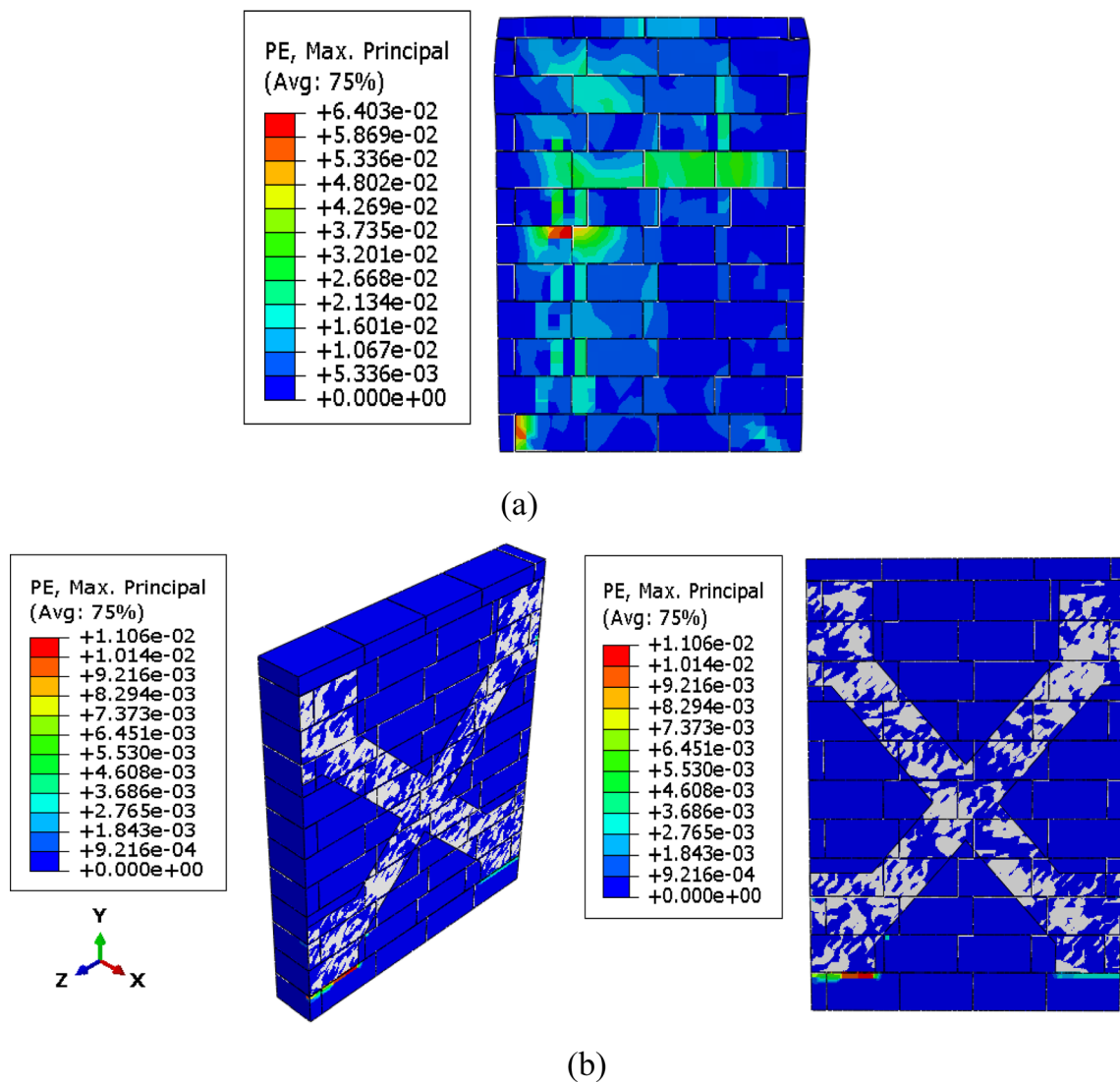

(a)

(b)

Fig. 20 Maximum principal plastic strains a Model-W1 and b Model-W2

The maximum difference ratio between the numerical and experimental load-bearing capacity values for both models is 3.63%. Similarly, the maximum displacement difference ratio is also acceptable, with a maximum of 3.00%. These results indicate that the numerical model is effective in predicting the behavior of masonry infill walls subjected to cyclic loading. Therefore, the validation study confirmed that the developed FE micro-model could effectively predict the lateral capacity and crack pattern for each case. The numerical modeling predicted quite well the results of the in-plane quasi-static test.

A contour plot displaying the maximum principal (tensile) stresses and minimum principal (compressive) stresses at the initial peak point for both the damaged and strengthened cases is illustrated in Figs. 18 and 19, respectively. In the damaged case, the compressive stresses primarily localize along the loaded diagonal, as depicted in Fig. 18a. These minimum principal stress values occur only in a small and few local areas where they exceed the wall compressive strength, as detailed in Table 1. Simultaneously, in the center and upper left of the wall, principal tensile stresses are observed (Fig. 18b). As expected, the highest tensile stress obtained for the model was 0.39 MPa, which is over 0.22 and 0.15 MPa for the brick units and mortar, respectively. This stress value is considerably high, especially in comparison to the limited tensile strength of the wall.

Figure 19 depicts the maximum principal stress from the FE simulation results, indicating that the upper corner areas of the masonry wall are subjected to the highest stress, reaching 3.12 MPa. This value is slightly above the ultimate compressive stress of the brick. Nevertheless, it is slightly greater than the mortar strength as recorded in the testing data (Table 1). It is also important to illustrate that the tensile stress values obtained were below the tensile strength. The enhanced numerical masonry wall gained a higher load capacity due to the high tensile strength of the CFRP strips bonded to the wall surface.

The plastic strain diagram (PE) module in ABAQUS describes the accumulation result of plastic strain during the entire deformation process. According to Fig. 20a the value of plastic strain of Model-W1 is greater than 0, it means that the material has reached the yield capacity, which can approximate the location and state of wall cracks which might cause the failure.

In Fig. 20b, the cracks propagated along the head and bed joints and in the masonry units themselves of the unstrengthened region of Model-W2. These cracks resulted in the redistribution of tensile stresses over the uncracked regions. Plastic strain contours are a useful tool for understanding where plastic deformation is occurring within a material. While they may not directly represent cracks, they can provide insights into regions of high stress

and strain where cracks are more likely to initiate or propagate. It is noted here that plastic strains occur in the damaged areas of the wall, primarily due to tension.

5 Conclusions

A numerical study was conducted to evaluate and compare experimental findings on the in-plane behavior of masonry infill walls. The research focused on predicting dynamic characteristics such as frequency values and mode shapes, load–displacement hysteretic curves, damage patterns, and the stress distribution and contribution to its mode of failure. Based on the FE results, three different cases, such as undamaged, damaged, and strengthened models, were modeled and simulated using 3D-simplified micro-modeling through ABAQUS 2019. Based on this investigation, the following conclusions are presented:

- Model-W2, compared to its Model-W1, has enabled an increase in frequency values of about 57% in first mode. When comparing the CFRP strengthened to an undamaged case, there is an observed increase in frequency value of approximately 24%. This highlights the efficacy of CFRP in restoring the wall's strength capacities. Since the mass remains constant, the observed increase in strength can be attributed to the enhanced rigidity of the brick infill wall due to CFRP strengthening.
- When comparing numerical and experimental results for undamaged and strengthened cases, the outcomes are remarkably similar, with frequency discrepancies less than 1%. However, this similarity further intensifies in the case of damaged models, where the error percentages remain below 4%.
- Test results indicated that CFRP strips remarkably increase the flexural capacity of infill masonry walls. Moreover, the strengthening systems were effective in enhancing the stiffness of the strengthened model.
- The strength capacity of the Model-W2 was improved by 42% in the case of strengthening.
- The hysteresis curve of Model-W1 indicates that the maximum peak values reach approximately ±97 KN. The largest displacements on this curve fluctuate between 10 and 18 mm. However, one of these peaks is attained at a displacement of 9.55 mm.
- The maximum loads at which peaks are obtained range between 130 and 136 KN. This indicates an enhancement in the mechanical properties of the wall due to the application of CFRP.
- The numerical results for dynamic characteristics, such as frequency values and mode shapes, show a promising correlation with experimental data. The average

discrepancies in frequency values are calculated to be 0.75% for Model-W0, 3.87% for Model-W1, and 0.99% for Model-W2. This close alignment suggests that the FE model is sufficiently accurate for practical engineering applications.

- The analysis results demonstrate that the constituted FE model software can predict the load-bearing capacity and maximum displacement values of masonry infill walls under cyclic loading with high accuracy, with a maximum difference ratio of less than 4% for Model-W1 and Model-W2.

- The simplified micro-modeling model without and with strengthened masonry infill walls demonstrated computational efficiency while maintaining accurate prediction of nonlinear behavior under the cyclic loading protocol.

- The results obtained from the nonlinear dynamic analysis indicate that compression at the corners, shear sliding, and diagonal tension failure modes that can occur in the infill wall are highly vulnerable to seismic loads.

- In scenarios involving both damaged and strengthened walls, the minimum and maximum principal stress values decrease by factor times of 0.8 and 2, respectively. These stress values do not exceed the strength capacity of the brick masonry, though they slightly exceed the mortar's strength. This suggests potential for enhancement of the model through increased CFRP strip-to-masonry infill wall. Additionally, it is noted that the distribution of maximum principal stress is predominantly concentrated in the unstrengthened areas of Model-W2.

These findings suggest that the numerical FE model has significant potential for designing and strengthening models for improved seismic performance. Despite the fact that masonry infill walls exhibit complex behavior due to the distinct material properties and geometries of the brick unit, mortar, steel frame, and CFRP layer, the nonlinear finite element analysis outcomes are in agreement with the experimental test results.

References

1. Liu Y, Manesh P (2013) Concrete masonry infilled steel frames subjected to combined in-plane lateral axial loading: an experimental study. Eng Struct 52:331–339

2. Haach VG, Vasconcelos G, Lourenço PB (2010) Experimental analysis of reinforced concrete block masonry walls subjected to in-plane cyclic loading. J Struct Eng 136(4):452–462

3. Mehrabi AB, Shing PB (1997) Finite element modeling of masonry-infilled RC frames. J Struct Eng 123(5):604–613

4. Chen X, Liu Y (2015) Numerical study of in-plane behaviour strength of concrete masonry infills with openings. Eng Struct 82:226–235

5. Koutromanos I, Stavridis A, Shing PB, Willam K (2011) Numerical modeling of masonry-infilled RC frames subjected to seismic loads. Comput Struct 89(11–12):1026–1037

6. Chengcheng Z, Li L, Haihong L (2018) Dynamic analysis of horizontal inlay reinforcement based on ABAQUS masonry structure. Value Eng 37(12):122–124

7. Buonopane SG, White RN (1999) Pseudodynamic testing of masonry infilled reinforced concrete frame. J Struct Eng 125(6):578–589

8. Žarnić R, Gostič S, Crewe AJ, Taylor CA (2001) Shaking table tests of 1: 4 reduced-scale models of masonry infilled reinforced concrete frame buildings. Earthq Eng Struct Dyn 30(6):819–834

9. Hashemi A, Mosalam KM (2006) Shake-table experiment on reinforced concrete structure containing masonry infill wall. Earthq Eng Struct Dyn 35(14):1827–1852

10. Asteris PG, Repapis CC, Repapi EV, Cavaleri L (2017) Fundamental period of infilled reinforced concrete frame structures. Struct Infrastruct Eng 13(7):929–941

11. Di Sarno L, Wu JR (2020) Seismic assessment of existing steel frames with masonry infills. J Constr Steel Res 169:106040

12. Asteris PG, Cavaleri L, Di Trapani F, Tsaris AK (2017) Numerical modelling of out-of-plane response of infilled frames: state of the art future challenges for the equivalent strut macro-models. Eng Struct 132:110–122

13. Tasnimi AA, Mohebkhah A (2011) Investigation on the behavior of brick-infilled steel frames with openings, experimental analytical approaches. Eng Struct 33(3):968–980

14. Faraji Najarkolaie K, Mohammadi M, Fanaie N (2017) Realistic behavior of infilled steel frames in seismic events: experimental analytical study. Bull Earthq Eng 15:5365–5392

15. Di Sarno L, Freddi F, D'Aniello M, Kwon OS, Wu JR, Gutierrez-Urzua F, Strepelias E (2021) Assessment of existing steel frames: numerical study, pseudo-dynamic testing influence of masonry infills. J Constr Steel Res 185:106873

16. Mehrabi AB, Benson Shing P, Schuller MP, Nol JL (1996) Experimental evaluation of masonry-infilled RC frames. J Struct Eng 122(3):228–237

17. Canbay E (2001) Contribution of RC infills to the seismic behavior of structural systems. PhD Dissertation, University of Middle East Technical

18. Anil O, Altin S (2006) An experimental study on reinforced concrete partially infilled frames. Eng Struct 29(2007):449–460

19. Darwish MMSED (2006) Numerical modeling of infill RC walls in seismic retrofit of RC frames. Doctoral dissertation, University of American

20. Sivri M, Demir F, Kuyucular A (2006) The effects of infill walls, frame structures on the earthquake behavior failure mechanism. J Inst Nat Sci 10(1):109–115

21. Lotfi HR, Shing PB (1994) Interface model applied to fracture of masonry structures. J Struct Eng 120(1):63–80

22. Al-Chaar G, Mehrabi AB, Manzouri T (2008) Finite element interface modeling experimental verification of masonry-infilled R/C frames Longmont. Masonry Society, CO, USA

23. Stavridis A, Shing PB (2010) Finite-element modeling of nonlinear behavior of masonry-infilled RC frames. J Struct Eng 136(3):285–296

24. Mohyeddin A, Goldsworthy HM, Gad EF (2013) FE modelling of RC frames with masonry infill panels under in-plane out-of-plane loading. Eng Struct 51:73–87

25. Minaie E, Moon FL, Hamid AA (2014) Nonlinear finite element modeling of reinforced masonry shear walls for bidirectional loading response finite elements in analysis. Design 84:44–53

26. Kim M, Yu E (2021) Experimental study on lateral-load-resisting capacity of masonry-infilled reinforced concrete frames. Appl Sci 11(21):9950

27. Caliò I, Pantò B (2014) A macro-element modelling approach of infilled frame structures. Comput Struct 143:91–107

28. Peng X, Gu Q (2013) Seismic behavior analysis for composite structures of steel frame-reinforced concrete infill wall. Struct Des Tall Spec Build 22(11):831–846

29. Zhai CH, Kong JC, Wangm XM, Wang XH (2018) Finite-element analysis of out-of-plane behaviour of masonry infill walls. Proc Inst Civil Eng Struct Build 171(3):203–215

30. Kubalski T, Marinković M, Butenweg C (2016) Numerical investigation of masonry infilled RC frames. In: 16th International Brick Block Masonry Conference, pp 26–30

31. Yekrangnia M, Asteris PG (2020) Multi-strut macro-model for masonry infilled frames with openings. J Build Eng 32:101683

32. Markulak D, Dokšanović T, Radić I, Miličević I (2018) Structurally environmentally favorable masonry units for infilled frames. Eng Struct 175:753–764

33. Cavaleri L, Di Trapani F, Asteris PG, Sarhosis V (2017) Influence of column shear failure on pushover based assessment of masonry infilled reinforced concrete framed structures: a case study. Soil Dyn Earthq Eng 100:98–112

34. Nasiri E, Liu Y (2019) The out-of-plane behaviour of concrete masonry infills bounded by reinforced concrete frames. Eng Struct 184:406–420

35. Minga E, Macorini L, Izzuddin BA, Calio I (2020) 3D macroelement approach for nonlinear FE analysis of URM components subjected to in-plane out-of-plane cyclic loading. Eng Struct 220:110951

36. Azariani MG, Ghanbari-Ghazijahani T, Mohebkhah A, Classen M (2021) Concrete- timber-filled tubes under axial compression. Numerical theoretical study. J Build Eng 44:103231

37. Tabeshpour MR, Azad A, Golafshani, AA (2012) Seismic behavior retrofit of infilled frames. Earthquake-Resistant Structures-Design, Assessment Rehabilitation

38. Binici B, Ozcebe G (2006) Seismic evaluation of infilled reinforced concrete frames strengthened with FRPS. In: Proceedings of the 8th US national conference on earthquake engineering

39. Batikha M (2008) Strengthening of thin metallic cylindrical shells using fibre reinforced polymers

40. Yuksel E, Ozkaynak H, Buyukozturk O, Yalcin C, Dindar AA, Surmeli M, Tastan D (2010) Performance of alternative CFRP retrofitting schemes used in infilled RC frames. Constr Build Mater 24(4):596–609

41. Ozkaynak H, Yuksel E, Buyukozturk O, Yalcin C, Dindar AA (2011) Quasi-static pseudo-dynamic testing of infilled RC frames retrofitted with CFRP material. Compos B Eng 42(2):238–263

42. Altin S, Anil Ö, Kara ME, Kaya M (2008) An experimental study on strengthening of masonry infilled RC frames using diagonal CFRP strips. Compos B Eng 39(4):680–693

43. Butenweg C, Marinković M, Kubalski T, Klinkel S (2016) Masonry infilled reinforced concrete frames under horizontal loading. Stahlbetonrahmen mit Ausfachungen aus Mauerwerk unter horizontalen Belastungen. Mauerwerk 20(4):305–312

44. Akın E, Özcebe G, Canbay E, Binici B (2014) Numerical study on CFRP strengthening of reinforced concrete frames with masonry infill walls. J Compos Constr 18(2):04013034

45. Li T, Silva PF, Belarbi A, Nanni A, Myers JJ (2001) Retrofit of un-reinforced infill masonry walls with FRP. J Compos Constr 5:559–5637

46. Arifuzzaman S, Saatcioglu M (2012) Seismic retrofit of load bearing masonry walls by FRP sheets. In: Proceedings of the 15th world conference on earthquake engineering

47. Proença JM, Gago AS, Costa AV (2012) Strengthening of masonry wall load bearing structures with reinforced plastering mortar solution. In: Proceedings of the 15th world conference on earthquake engineering (15WCEE), Lisbon

48. Padalu PKVR, Singh Y, Das S (2020) Cyclic two-way out-of-plane testing of unreinforced masonry walls retrofitted using composite materials. Constr Build Mater 238:117784

49. Leeanansaksiri A, Panyakapo P, Ruangrassamee A (2018) Seismic capacity of masonry infilled RC frame strengthening with expanded metal ferrocement. Eng Struct 159:110–127

50. Coccia S, Di Carlo F, Imperatore S (2020) Masonry walls retrofitted with vertical FRP rebars. Buildings 10(4):72

51. Tanjung J, Ismail FA, Putra R (2020) A simple method for strengthening the brick masonry infilled in the reinforced concrete frame structure. Geomate J 18(66):118–123

52. Furtado A, Rodrigues H, Arêde A, Varum H (2020) Experimental tests on strengthening strategies for masonry infill walls: a literature review. Constr Build Mater 263:120520

53. Samberou AMS (2021) Masonry walls behavior determination under cyclic loads by experimental finite element method strengthening with FRP material. Phd Dissertation, University of Karadeniz Technical

54. Release 112 Bruel Kjaer (2006) Sound vibration measurement A/S PULSE analyzers Solutions, Denmark

55. Release 40 (2006) Structural Vibration Solution A/S OMA, Denmark

56. FEMA (2007) Interim testing protocols for determining the seismic performance characteristics of structural nonstructural components FEMA 461, Washington

57. Dhakal RP, Pourali A, Tasligedik AS, Yeow T, Baird A, MacRae G, Palermo A (2016) Seismic performance of non-structural components contents in buildings: an overview of NZ research. Earthq Eng Eng Vib 15:1–17

58. ABAQUS (2019) Inc ABAQUS 2019 User's Manual Dassault Systèmes Simulia Corp

59. Narayanan SP, Sirajuddin M (2013) Properties of brick masonry for FE modeling. Am J Eng Res 1:6–11

60. Liu Z, Crewe A (2020) Effects of size position of openings on in-plane capacity of unreinforced masonry. Bull Earthq Eng 18(10):4783–4812

61. ASTM Stard A36 (2008) Stard Specification for Structural Steel ASTM International, West Conshohocken, PA. 101520/A0036_A0036M-08. www.astm.org

62. Lee J, Fenves GL (1998) Plastic-damage model for cyclic loading of concrete structures. J Eng Mech 124(8):892–900

63. Lourenço PB, Rots JG, Der V, Pluijm R (1999) Understing the tensile behavour of masonry parallel to the bed joints: a numerical approach. Masonry Int 12(3):96–103

64. Moradabadi E, Laefer DF, Clarke JA, Lourenço PB (2015) A semi-rom field finite element method to predict the maximum eccentric compressive load for masonry prisms. Constr Build Mater 77:489–500

65. Page A (1981) The biaxial compressive strength of brick masonry In: ICE proceedings, vol 3. Thomas Telford, pp 893–906

66. Belarbi A, Hsu TT (1994) Constitutive laws of concrete in tension reinforcing bars stiffened by concrete. Struct J 91(4):465–474

67. Lubliner J, Oliver J, Oller S, Oñate E (1989) A plastic-damage model for concrete. Int J Solids Struct 25(3):299–326

68. Silva LM, Christoforo AL, Carvalho RC (2021) Calibration of concrete damaged plasticity model parameters for shear walls. Rev Matér 26

69. Yazdani M, Habibi H (2023) Residual capacity evaluation of masonry arch bridges by extended finite element method. Struct Eng Int 33(1):183–194

70. Tiberti S, Acito M, Milani G (2016) Comprehensive FE numerical insight into Finale Emilia Castle behavior under 2012 Emilia Romagna seismic sequence: damage causes seismic vulnerability mitigation hypothesis. Eng Struct 117:397–421

71. Belakhdar K, Tounsi A (2015) Finite element analysis of initially damaged beams repaired with FRP plates. Compos Struct 134:429–439

72. Bustamante-Góez L, Chica-Arrieta E, Villarraga-Ossa J (2019) Assessment of cohesive traction-separation relationship according stiffness variation. Revista UIS Ingenierías 18(2):67–76

73. Peng Q, Zhou X, Yang C (2018) Influence of connection constructional details on masonry-infilled RC frames under cyclic loading. Soil Dyn Earthq Eng 108:96–110

74. Karnati SR, Shivakumar K (2020) Limited Input Benzeggagh Kenane delamination failure criterion for mixed-mode loaded fiber reinforced composite laminates. Int J Fract 222(1–2):221–230

75. Diehl T (2005) Modeling surface-bonded structures with ABAQUS cohesive elements: beam-type solutions In: ABAQUS users' conference, pp 1–27

76. Aref AJ, Dolatshahi KM (2013) A three-dimensional cyclic meso-scale numerical procedure for simulation of unreinforced masonry structures. Comput Struct 120:9–23

77. Zhang M, Ding J, Pang L, Ding K (2023) Numerical study on the influence of in-plane damage on the out-of-plane seismic performance of masonry infill walls with opening in reinforced concrete frames. Adv Struct Eng 26(2):344–359

78. Abdulla KF, Cunningham LS, Gillie M (2017) Simulating masonry wall behaviour using a simplified micro-model approach. Eng Struct 151:349–365

79. Dhir PK, Tubaldi E, Ahmadi H, Gough J (2021) Numerical modelling of reinforced concrete frames with masonry infills rubber joints. Eng Struct 246:112833

80. Yee SS, Kong KH, Liew RJY (2023) Numerical analysis of reinforced concrete composite wall under concentric axial loading. In: Proceedings of the 17th East Asian-Pacific conference on structural engineering construction, 2022: EASEC-17, Singapore. Springer Nature Singapore, Singapore, pp 1087–1100

81. Karimi AH, Karimi MS, Kheyroddin A, Shahkarami AA (2016) Experimental numerical study on seismic behavior of an infilled masonry wall compared to an arched masonry wall. Structures 8:144–153

82. Mahmod FHRW, Kareem KM, Ahani E, Ahmmad BS (2022) Appraising 2D discrete macro element model of masonry infill wall using ABAQUS CAE software. In: 2022 8th International engineering conference on sustainable technology development (IEC). IEEE, pp 83–88

83. Wei MW, Richard Liew JY, Fu XY (2019) Nonlinear finite element modeling of novel partially connected buckling-restrained steel plate shear walls. Int J Steel Struct 19:28–43

84. Zhou Y, Pei Y, Zhou Y, Hwang HJ, Yi W (2020) Field measurements for calibration of simplified models of the stiffening effect of infill masonry walls in high-rise RC framed shear-wall buildings. Earthq Eng Eng Vib 19:87–104

85. Yazdani M (2021) Three-dimensional nonlinear finite element analysis for load-carrying capacity prediction of a railway arch bridge. Int J Civ Eng 19:823–836